Searches for mass-asymmetric compact binary coalescence events using neural networks in the LIGO/Virgo third observation period

M. Andrés-Carcasona,[1,*] A. Menéndez-Vázquez,[1] M. Martínez,[1,2] and Ll. M. Mir[1]

[1]*Institut de Física d'Altes Energies (IFAE), The Barcelona Institute of Science and Technology, Campus UAB, E-08193 Bellaterra (Barcelona), Spain*

[2]*Catalan Institution for Research and Advanced Studies (ICREA), E-08010 Barcelona, Spain*

(Received 6 December 2022; accepted 8 March 2023; published 17 April 2023)

We present the results of the search for the coalescence of compact binary mergers with very asymmetric mass configurations using convolutional neural networks and the Laser Interferometer Gravitational Wave Observatory/Virgo data for the third observation period (O3). Two-dimensional images in time and frequency are used as input. Masses in the range of $0.01 - 20M_{\odot}$ are considered. We explore neural networks trained with input information from a single interferometer, pairs of interferometers, or all three interferometers together, indicating that the use of the maximum information available leads to an improved performance. A scan over the O3 dataset using the convolutional neural networks for detection results in no significant excess from an only noise hypothesis. The results are translated into 90% confidence level upper limits on the merger rate as a function of the mass parameters of the binary system.

DOI: 10.1103/PhysRevD.107.082003

I. INTRODUCTION

Since the discovery of gravitational waves (GWs) in 2015 [1], generated by a compact binary coalescence (CBC) of black holes (BHs), the Laser Interferometer Gravitational Wave Observatory (LIGO) and Virgo experiments have improved their sensitivity and observed an increasing number of GW signals, including also events attributed to the coalescence of neutron stars (NSs), as well as the coalescence of BH-NS binary systems. The latest catalog of events, from the first through third observation runs (O1, O2, and O3), collects a total of 90 events, dominated by BH-BH candidates [2–4]. The data indicate that the masses in the binary systems range between $1.17M_{\odot}$ (GW191219_163120) and $105M_{\odot}$ (GW190426_190642), with a mass ratio $q \equiv m_1/m_2$, where m_1 denotes the heaviest of the two objects, in the range between 1.1 (GW170817) and 26.5 (GW191219_163120). The LIGO and Virgo Collaborations use matched-filtering techniques to extract the events from the much larger background (for a comprehensive review of the experimental techniques, see Ref. [5]). The use of machine learning tools has been extensively explored in LIGO and Virgo (for a comprehensive review, see Refs. [6,7]). In particular, the presence of a distinct chirplike shape in the CBC events, when represented in spectrograms showing the signal in the frequency-time domain, makes the use of a convolutional neural network (CNN) a valid alternative suitable for GW detection [8–17]. In addition, the use of CNNs has been explored to distinguish between families of glitches or cleaning the data [18–21].

In this paper, we explore the implementation of a CNN for the identification of CBC events with very asymmetric mass configurations with $q < 2000$, and m_1 and m_2 in the range between $1–20M_{\odot}$ and $0.01–1M_{\odot}$, respectively. This is motivated by the search for CBC candidates with the presence of subsolar-mass (SSM) BHs. Since there is no well-established astrophysical explanation for the origin of SSM BHs, their discovery would point to the presence of new physics. The presence of SSM BHs is predicted by different models, including primordial black holes from the collapse of overdensities in the early Universe [22–25], gravitational collapse of dark matter halos [26–29], the accumulation of dark matter by neutron stars leading to SSM BHs [30], or SSM boson stars [31–33]. As illustrated in Fig. 1, this study complements the phase space in mass considered by previous searches for SSM events using O3 data and matched-filtering-based selections [4,34–36]. Previous results using other observational periods are included in Refs. [37–40].

II. DATA PREPARATION

The study uses the O3 data from LIGO-Hanford (H1), LIGO-Livingston (L1), and Virgo (V1) interferometers with 4096 Hz sampling rate. After imposing quality requirements, dealing with the understanding of the interferometer stationary noise budget, as well as the identification and suppression of glitches and spectral noise contributions (for a comprehensive discussion, see Refs. [41,42]),

*Corresponding author.
mandres@ifae.es

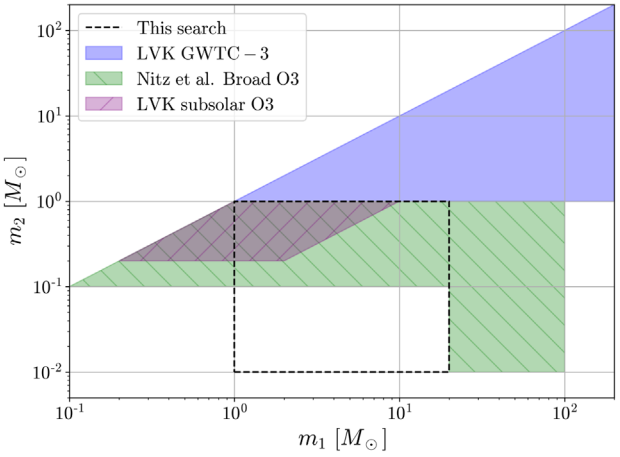

FIG. 1. Region of interest compared to other recent searches. The blue region is the one searched by the LVK Collaboration as part of the GWTC-3 catalog [4], the magenta hatched region corresponds to the LVK subsolar mass targeted search performed over O3 data [34,36], while the green hatched region corresponds to the broad search performed by Nitz and Wang over the O3 data [35].

the H1-L1-V1 combined samples have a total duration of 155 days. The H1-L1-V1 O3 data are used for constructing an image containing a spectrogram with only background and background plus injected signal for the purposes of the CNN training. Special precaution was taken in the preparation of the background images to exclude any of the identified GW events in O3, as collected in the third Gravitational-Wave Transient Catalog (GWTC-3) [4]. A total of 142,944 images was used. The results obtained (see below) show that this number of images is enough for an adequate training and validation of the network. The images are divided as follows: 115,200 (80.6%) for training, 12,800 (9.0%) for validating, and 14,944 (10.4%) for testing, evenly distributed into background-only and background with a signal injected.

Waveforms for GW signals are generated using PyCBC [43–45] with the IMRPhenomD [46,47] model and combined with data segments from the different interferometers, after taking into account the proper relative orientations, times of arrival, and antenna factors. This waveform family is not fully calibrated for the whole parameter space considered and, in particular, for large q. However, the use of very different waveform families results in a small impact on the spectrograms themselves, as input to the neural network, which is able to detect the event as long as the signal remains visible on the two-dimensional image. The parameters considered are uniformly sampled, as described in Table I, and zero spin components are assumed. Masses in the range between 1 and $20M_\odot$ (0.01 and $1M_\odot$) are considered for m_1 (m_2), and the corresponding luminosity distance D_L is limited to nearby events in the range 1–100 Mpc. Other parameters related to the position in the sky and orientation of the source are taken as homogeneously distributed.

TABLE I. Range of the uniformly sampled variables for the training set, (m_1, m_2) being the component masses, D_L the luminosity distance, ψ the inclination of the orbit with respect to the line of sight, θ_{JN} the polarization of the gravitational wave, and (α, δ) the right ascension and declination, respectively.

$m_1(M_\odot)$	$m_2(M_\odot)$	D_L(Mpc)	ψ	θ_{JN}	α	$\cos(\delta)$
[1, 20]	[0.01, 1]	[1, 100]	$[0, \pi/2]$	$[0, \pi]$	$[0, 2\pi]$	$[-1, 1]$

The injected signals are limited to a fixed maximum duration of 5 s. The 5-s window is computed backward from the merger time to remove low-amplitude monochromaticlike parts of the waveform and avoid confusing the network during training. A low-frequency threshold of 45 Hz is applied in order to control the duration of the injected signal. Finally, the signals are randomly placed within the 5-s window. Once the GW signals are injected in the different H1, L1, and V1 background segments, the data are processed. First, the time series is whitened following the same prescription as in Refs. [5,48]. Two-dimensional arrays holding spectrogram data are then produced using Q transforms [49–51] in order to arrive at the desired images in terms of amplitude vs time vs frequency, with 400 bins in time and 100 bins in frequency. Figure 2 presents an example of spectrograms corresponding to a binary BH event with $m_1 = 2.6M_\odot$ and $m_2 = 0.35M_\odot$ at a distance of 3.4 Mpc. In the case of H1 and L1, the characteristic chirp is clearly observed.

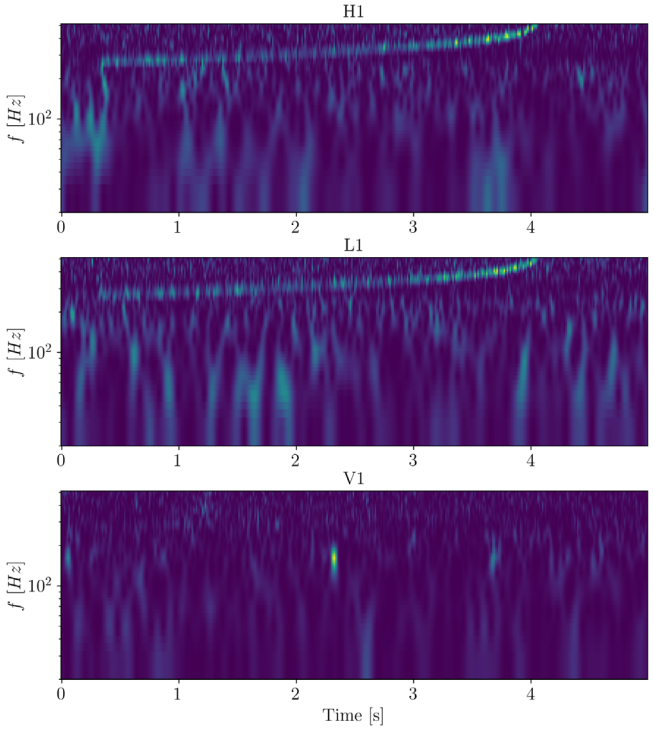

FIG. 2. Spectrograms for a binary system with $m_1 = 2.6M_\odot$ and $m_2 = 0.35M_\odot$ and a distance $D_L = 3.4$ Mpc, as seen in H1, L1, and V1.

In order to account for the presence of glitches in the data, not completely suppressed by the whitening process and leading to instabilities in the CNN training [52], the contents in each image are renormalized in such a way that they have an average equal to 0 and a variance equal to 1, following the same prescription as in Ref. [12].

III. NEURAL NETWORK DEFINITION AND TRAINING

This study closely follows that of Ref. [12], using a ResNet50 architecture [53,54] (see Table II) with modifications in the last layer, for which average pooling and a fully connected dense layer (1-d fc) with a sigmoid activation function are implemented. For the loss function, a binary cross-entropy is employed. Finally, a learning rate of 0.01 alongside an Adam optimizer [55–57] and a batch size of 32 are used for a total of 10 epochs. With all these parameters, different CNNs have been trained using the graphics processing unit enhanced capabilities of KERAS and TensorFlow [58].

We train seven different CNNs. Three CNNs are trained separately for H1, L1, and V1 data. In addition, three CNNs are trained for H1-L1, H1-V1, and L1-V1 pairs of input data, and one CNN is trained for H1-L1-V1 combined input data, where information from two or three interferometers

TABLE II. CNN architecture and the associated hyperparameters. Building blocks are shown in brackets, with the numbers of blocks stacked. Downsampling is performed by conv3_1, conv4_1, and conv5_1 with a stride of 2 (partially taken from [53]).

Layer name	Output size	Layer structure
Conv1	112×112	7×7, 64, stride 2
		3×3 max pool, stride 2
Conv2_x	56×56	$\begin{bmatrix} 1 \times 1, 64 \\ 3 \times 3, 64 \\ 1 \times 1, 256 \end{bmatrix} \times 3$
Conv3_x	28×28	$\begin{bmatrix} 1 \times 1, 128 \\ 3 \times 3, 128 \\ 1 \times 1, 512 \end{bmatrix} \times 4$
Conv4_x	14×14	$\begin{bmatrix} 1 \times 1, 256 \\ 3 \times 3, 256 \\ 1 \times 1, 1024 \end{bmatrix} \times 6$
Conv5_x	7×7	$\begin{bmatrix} 1 \times 1, 512 \\ 3 \times 3, 512 \\ 1 \times 1, 2048 \end{bmatrix} \times 3$
	1×1	Global average pool, 1-d fc, sigmoid

Hyperparameters	
Learning rate	0.01
Batch size	32
Number of epochs	10
Optimizer	Adam
Loss function	Binary cross-entropy

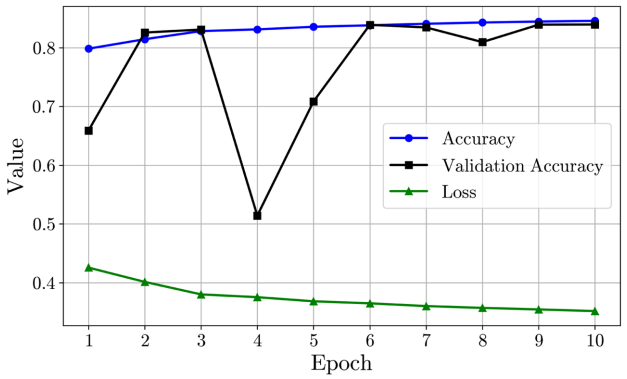

FIG. 3. Accuracy, loss, and validation accuracy during the training epochs for the H1-L1-V1 CNN.

are input simultaneously to the corresponding CNNs. This means that the input matrix will have dimensions $(400, 100, x)$ where $x = 1, 2, 3$ depending on the number of interferometers used. By feeding simultaneously the data from various interferometers to the CNN, we allow it to learn about the possible correlations present, and the final discriminant output by the CNN will already be aware of whether the signal is visible in multiple detectors or not. As expected, the performances of the CNNs improve by including the information of multiple interferometers during the training process, since the CNN learns about correlations across images in different channels when the signal is present. Therefore, CNNs using single interferometer information are discarded for the final scan over the O3 data.

Figure 3 shows, for the H1-L1-V1 case, the evolution of the accuracy and loss as a function of epochs, demonstrating stability after about 8–10 epochs, with an accuracy above 0.8 and a loss below 0.4. In addition, the validation accuracy is presented, demonstrating a healthy evolution of the training process. The final CNN output for the H1-L1-V1 case is shown in Fig. 4, where a clear discrimination is obtained between signal and background samples. Similar features in the training process and the distribution of the final CNN discriminant are observed in the rest of the CNNs.

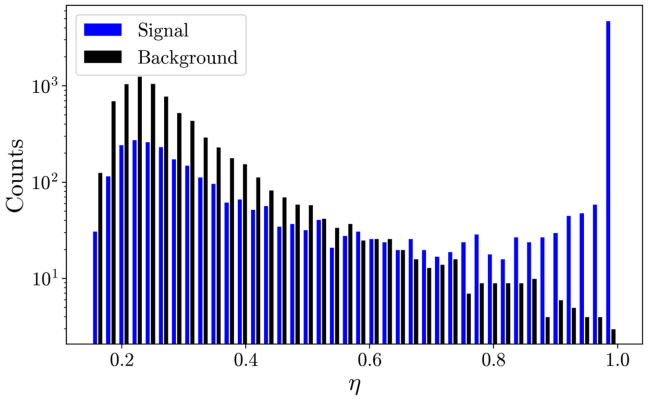

FIG. 4. CNN discriminating output corresponding to the H1-L1-V1 case for background and signal images.

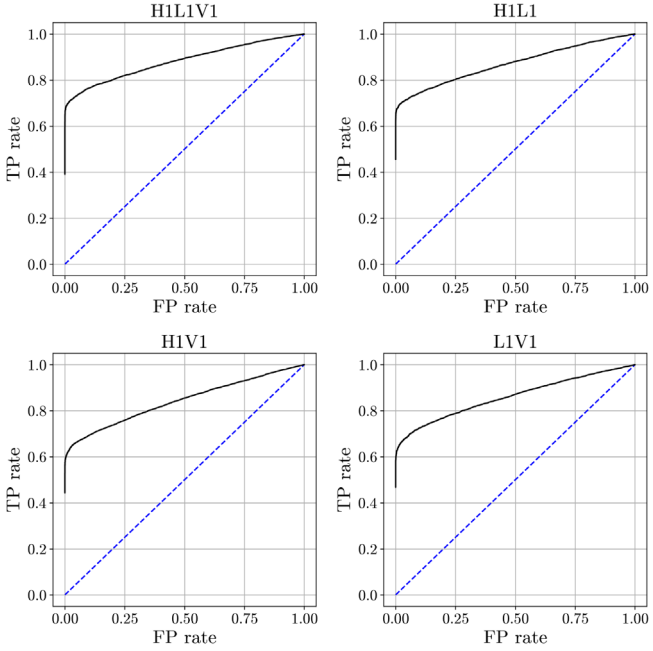

FIG. 5. ROC curves for the different CNNs.

The receiver operating characteristic (ROC) curves for the separate CNNs, representing the true positive (TP) versus the false positive (FP) rates, are presented in Fig. 5 for the H1-L1, H1-V1, L1-V1, and H1-L1-V1 CNNs. For very low FP rates, the TP rates only reach values around 70%, indicating a limited efficiency for event detection. The efficiency steadily increases at the cost of much larger FP rates. The ROC curve, along with a tolerable maximum false alarm rate (FAR) for detection, determines the final operating point of a given CNN. The computation of the FAR for each CNN follows the prescription in Ref. [1]. The FAR is defined as $\mathrm{FAR}(\eta) = N(\eta)/T$, where $\eta \in [0, 1]$ is the CNN discriminant output, $N(\eta)$ is the number of events with a CNN discriminant above or equal to η, and T is the period of time analyzed. In order to effectively increase the time considered in the calculation, reaching very low FAR values, the time slide technique [1,59] is used. This allows accumulating $\mathcal{O}(10^9)$ images of 5-s duration each and accessing FAR values down to $1/152.6\ \mathrm{yr}^{-1}$.

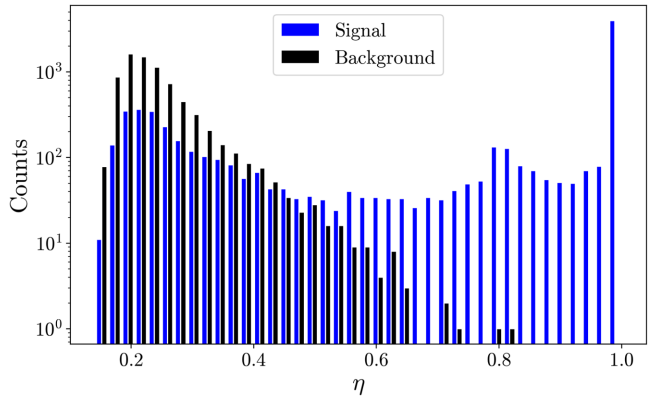

FIG. 6. CNN global discriminating output corresponding to the average of the H1-L1-V1, H1-L1, L1-V1, and H1-V1 CNN outputs for background and signal images.

TABLE III. Anticipated TP and FP rates and FAR for the different CNNs and a discriminant $\eta_0 = 1$. The FP rates represent a 95% confidence level upper limit according to a null observation of FP in the testing set assuming Poisson statistics.

CNN	Threshold	TP rate	FP rate	$\mathrm{FAR}(\eta_0 = 1)$ $[\mathrm{yr}^{-1}]$
H1—L1	1.0	0.46	$\leq 2 \times 10^{-4}$	$\sim 10^2$
L1—V1	1.0	0.47	$\leq 2 \times 10^{-4}$	$\sim 10^3$
H1—V1	1.0	0.44	$\leq 2 \times 10^{-4}$	$\sim 10^2$
H1—L1—V1	1.0	0.58	$\leq 2 \times 10^{-4}$	$\sim 10^3$
Combined	0.998	0.50	$\leq 2 \times 10^{-4}$	$\sim 10^{-2}$

We initially establish a CNN discriminant η_0 corresponding to a $\mathrm{FAR}(\eta_0)$ value of $1\ \mathrm{yr}^{-1}$. However, the number of FP detected remains sizable when $\eta_0 \to 1$ and the CNNs never reach a discriminant capable of producing only one false positive event per year. A further improvement of the global sensitivity is achieved by combining the outputs of the separate CNNs into a global discriminant. Such combination provides an additional tool for suppressing glitches in the data affecting independently the interferometers and in different time stamps. A simple average of the H1-L1-V1, H1-L1, L1-V1, and H1-V1 CNN outputs has been considered. Alternatively, a number of algorithms, potentially giving different weights to different CNNs, were explored leading to very similar or even worse results. The resulting discriminant is presented in Fig. 6 demonstrating an improved separation between background and signal, leading to a higher significance for the events finally selected as signal. Table III collects the corresponding detection rates and the computed FAR upper limit in the case of $\eta_0 = 1$ for the separate CNNs and their combination, where only the latter shows FAR values less than one event per year.

Signal injection studies are performed to establish the sensitivity of the different CNNs to the presence of a GW

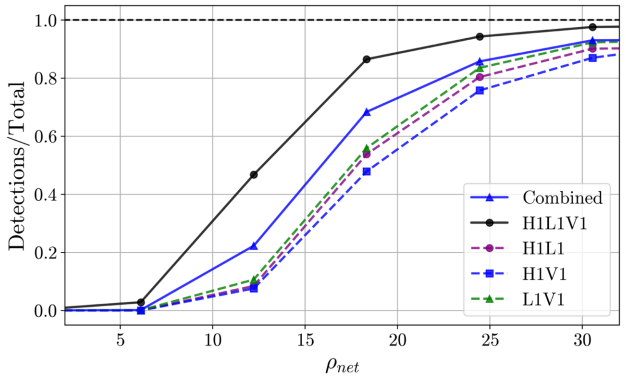

FIG. 7. Signal detection efficiency as a function of ρ_{net} for the different CNNs and their combination.

TABLE IV. Values of $\rho_{\rm net}$ at given detection efficiencies for the different CNNs and the combination of outputs.

CNN	$\rho_{\rm net}(80\%)$	$\rho_{\rm net}(90\%)$	$\rho_{\rm net}(95\%)$
H1—L1	24.4	30.5	42.0
L1—V1	23.7	29.0	41.2
H1—V1	26.8	21.1	25.8
H1—L1—V1	17.3	21.1	25.8
Combined	22.4	28.0	40.1

signal. For each GW signal, the signal-to-noise ratio (SNR) ρ is computed following the prescription in Ref. [8], solving the integral

$$\rho^2 = 4\int_{f_{\rm min}}^{f_{\rm max}} {\rm d}f \frac{|\tilde{h}(f)|^2}{S_n(f)}, \tag{1}$$

in the frequency domain (f), where $\tilde{h}(f)$ denotes the signal in the frequency domain and $S_n(f)$ is the power spectral density of the background. A Tukey window with $\alpha = 1/9$ is considered for the Fourier transform. The SNR defined above refers to each of the interferometers separately. Following the work in Refs. [60,61], when appropriate, we define a network SNR $\rho_{\rm net}$ as

$$\rho_{\rm net}^2 = \sum_i \rho_i^2, \tag{2}$$

where i denotes the different interferometers. Figure 7 shows the fraction of GW signals identified by the CNNs as a function of $\rho_{\rm net}$ in the different cases. As expected, the efficiency for signal detection increases rapidly with increasing SNR, becoming more efficient for large $\rho_{\rm net}$ values and improving with the inclusion of information from multiple interferometers. The best results are obtained by the H1-L1-V1 CNN. The result from the combination of CNNs is a compromise between the H1-L1-V1 CNN and the rest. Events with $\rho_{\rm net} \geq 25$ would be detected with an efficiency above 95% in the case of the H1-L1-V1 CNN. Table IV collects the values of $\rho_{\rm net}$ at given detection efficiencies for the different CNNs.

IV. RESULTS

We performed a scan of the full O3 dataset, using the H1-L1-V1 combined sample, for which a slicing window of 5-s duration was used in steps of 2.5 s (leading to a 50% overlap between consecutive images) in each of the interferometers. This translates into more than 80×10^6 images to be tested for the presence of potential signals. The CNN global discriminating output, defined as the average of the H1-L1-V1, H1-L1, L1-V1, and H1-V1 CNN outputs, is used to search for signal of SSM events. A scan over the data using different global discriminating values in the range between 0 and 1 is performed. In each case, the corresponding FAR is computed. The computation time for the entire O3 scan has been on the order of 2000 CPU hours

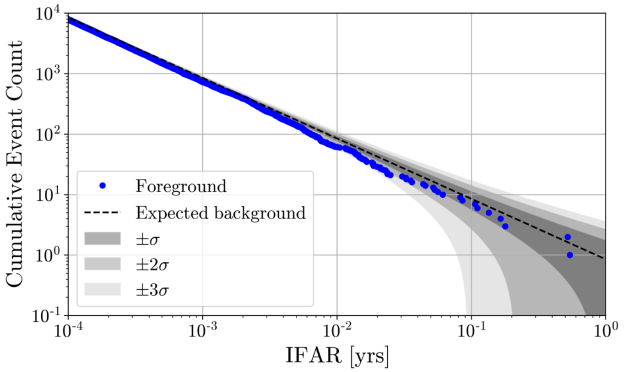

FIG. 8. Observed cumulative event count as a function of the inverse false alarm rate for the O3 scan (dots). The data are compared to foreground predictions (dashed line) and include 1σ, 2σ, and 3σ bands (shadowed areas).

(on an Intel Xeon CPU E5-2680 v4 @ 2.40 GHz). This represents a major improvement compared with the typically required CPU time for known matched-filtering pipelines.

The resulting inverse FAR distribution (IFAR), in units of years, is presented in Fig. 8 compared to the expected yield of noise events following a Poisson probability distribution. No significant deviation from the expected noise is observed and no claim of SSM event detection can be made. For illustration purposes, Fig. 9 shows the H1, L1, and V1 spectrograms for the most significant event having a FAR of 1.9 $\rm yr^{-1}$, a combined CNN value equal to 0.9635,

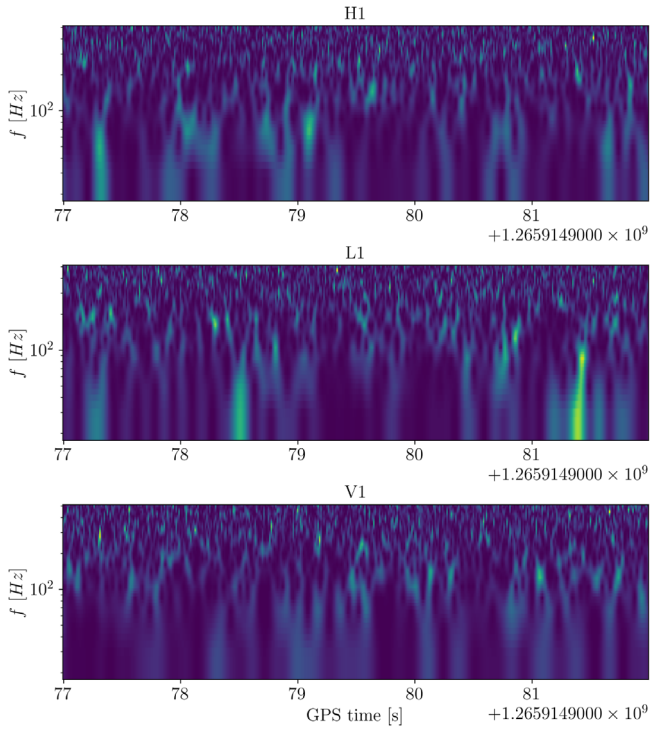

FIG. 9. Spectrogram of the most significant image. Corresponds to a FAR = 1.9 $\rm yr^{-1}$.

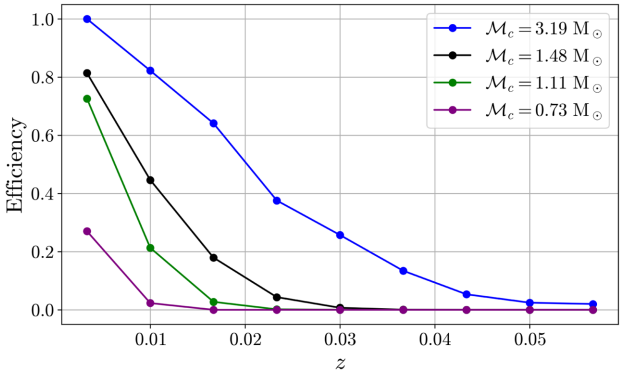

FIG. 10. Detection efficiency for the combined CNN discriminant as a function of z for different values of the chirp mass.

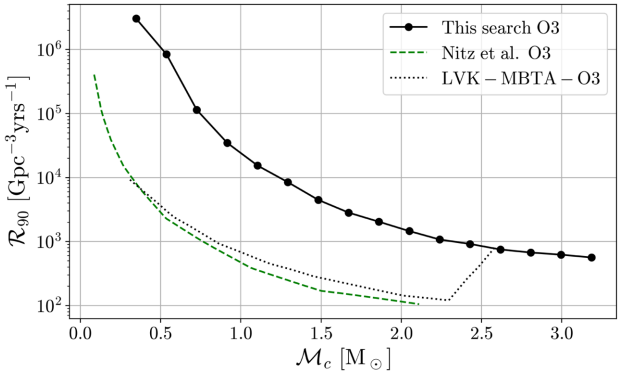

FIG. 11. The 90% confidence level upper limit on $\mathcal{R}_{90}$ as a function of the chirp mass. Our result (solid line) is compared with matched-filtering-based results from [35] (dashed line) and from [36] (dotted line). The curve in [36] presents a sudden increase in the last chirp mass bin, as the component masses contained in this bin are beyond the ones covered by their template bank.

and CNN values equal to 0.9848, 0.9172, 0.9774, and 0.9747 for the H1-L1-V1, H1-L1, L1-V1, and H1-V1 neural networks, respectively.

The results are translated into 90% confidence level (C.L.) upper limits of the merger rate of binary systems in the range of masses and q values considered. Since the sensitivity for detection mostly depends on the chirp mass of the binary system, defined as $\mathcal{M}_c \equiv \frac{(m_1 m_2)^{3/5}}{(m_1+m_2)^{1/5}}$, the computed merger rates are binned in $\mathcal{M}_c$ instead of in the single masses of the binary system. The 90% C.L. upper limits are calculated using the loudest event statistics approach [34–36,62,63] in terms of the surveyed time volume $\langle VT \rangle$, following the expression

$$\mathcal{R}_{90} = \frac{2.3}{\langle VT \rangle}, \qquad \langle VT \rangle = T \int \mathrm{d}z \frac{1}{1+z} \frac{\mathrm{d}V_c}{\mathrm{d}z} \varepsilon(z), \tag{3}$$

where T is the total observation time, z denotes the redshift, V_c is the comoving volume, and ε is the efficiency for detection. In this study, T is limited to 155 days when H1, L1, and V1 interferometers were all taking data simultaneously. Figure 10 presents the detection efficiency of the combined CNN discriminant as a function of z in several $\mathcal{M}_c$ bins. The efficiency is computed using injected signals and it vanishes for $z > 0.06$. The integral above is marginalized over the rest of parameters of the binary system (see Table I), which are considered homogeneously distributed in comoving volume.

Figures 11 and 12 present the 90% C.L. upper limits on the merging rate as a function of the chirp mass and as a function of m_2 in different m_1 regions, respectively. The results are compared to similar ones obtained with matched-filtering techniques. Our result provides 90% C.L. upper limits in the range between 3×10^6 and 560 Gpc^{-3} yr^{-1} with increasing chirp mass, extending previous results to chirp masses up to $3M_\odot$. At lower chirp mass, our constraints are weaker than previous results. This is partially attributed to the effective reduction of the observation time, by a factor of about 2, from limiting the data to simultaneous H1-L1-V1 configurations, as a way to obtain manageable false alarm rates. As shown in Fig. 12, the constraints from our analysis are more stringent with increasing mass difference $m_1 - m_2$, as expected for a CNN trained on very asymmetric configurations.

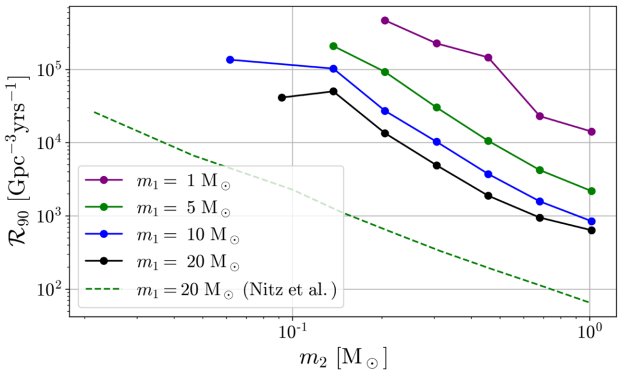

FIG. 12. The 90% confidence level upper limit on $\mathcal{R}_{90}$ as function of m_2 in different m_1 regions. Our result (solid lines) is compared with results of Nitz and Wang [35] (dashed line).

V. CONCLUSIONS

We present the results of a search for compact binary coalescence events with asymmetric mass configurations with masses in the range $0.01 - 1M_\odot$ for the lighter object and $1 - 20M_\odot$ for the heavier, using LIGO-Virgo O3 data and dedicated convoluted neural networks based on the analysis of frequency-time spectrograms. Different neural networks and a combination of them are explored, involving the simultaneous use of data from several interferometers. The scan over the O3 data results in no significant signal events found. The CNN approach for scanning the data is found to be much faster than traditional matched-filtering-based pipelines. The CNN results are translated

into 90% confidence level upper limits on the merger rates as a function of the mass parameters of the binary system for events of $z < 0.06$ and for the trained range. Although the results do not improve other bounds using matched-filtering techniques, partially due to the limited observation time considered, the CNN approach allows for effectively extending the search toward larger chirp masses.

ACKNOWLEDGMENTS

The authors are grateful for computational resources provided by PIC (Spain) and by the LIGO Laboratory supported by the National Science Foundation. The authors thankfully acknowledge the computer resources at MinoTauro and the technical support provided by Barcelona Supercomputing Center (RES-FI-2021-3-0020). This work is partially supported by the Spanish MCIN/AEI/10.13039/501100011033 under the Grants No. SEV-2016-0588, No. PGC2018-101858-B-I00, and No. PID2020-113701GB-I00, some of which include ERDF funds from the European Union, and by the MICIIN with funding from the European Union NextGenerationEU (PRTR-C17.I1) and by the Generalitat de Catalunya. IFAE is partially funded by the CERCA program of the Generalitat de Catalunya. M. A.-C. is supported by the 2022 Grant No. FI-00335 from the Generalitat de Catalunya.

[1] B. Abbott *et al.* (LIGO Scientific Collaboration and Virgo Collaboration), Observation of Gravitational Waves from a Binary Black Hole Merger, Phys. Rev. Lett. **116**, 061102 (2016).
[2] R. Abbott *et al.* (LIGO Scientific Collaboration and Virgo Collaboration), GWTC-1: A Gravitational-Wave Transient Catalog of Compact Binary Mergers Observed by LIGO and Virgo during the First and Second Observing Runs, Phys. Rev. X **9**, 031040 (2019).
[3] R. Abbott *et al.* (LIGO Scientific Collaboration and Virgo Collaboration), GWTC-2: Compact Binary Coalescences Observed by LIGO and Virgo During the First Half of the Third Observing Run, Phys. Rev. X **11**, 021053 (2020).
[4] R. Abbott *et al.*, GWTC-3: Compact Binary Coalescences Observed by LIGO and Virgo During the Second Part of the Third Observing Run, arXiv:2111.03606.
[5] B. P. Abbott *et al.* (LIGO Scientific Collaboration and Virgo Collaboration), A guide to LIGO–Virgo detector noise and extraction of transient gravitational-wave signals, Classical Quantum Gravity **37**, 055002 (2020).
[6] E. Cuoco, J. Powell, M. Cavaglià, K. Ackley, M. Bejger, C. Chatterjee, M. Coughlin, S. Coughlin, P. Easter, R. Essick *et al.*, Enhancing gravitational-wave science with machine learning, Mach. Learn. **2**, 011002 (2021).
[7] E. A. Huerta and Z. Zhao, *Advances in Machine and Deep Learning for Modeling and Real-Time Detection of Multi-messenger Sources* (Springer, Singapore, 2020), pp. 1–27.
[8] H. Gabbard, M. Williams, F. Hayes, and C. Messenger, Matching Matched Filtering with Deep Networks for Gravitational-Wave Astronomy, Phys. Rev. Lett. **120**, 141103 (2018).
[9] D. George and E. A. Huerta, Deep neural networks to enable real-time multimessenger astrophysics, Phys. Rev. D **97**, 044039 (2018).
[10] T. D. Gebhard, N. Kilbertus, I. Harry, and B. Schölkopf, Convolutional neural networks: A magic bullet for gravitational-wave detection?, Phys. Rev. D **100** (2019).
[11] D. George and E. A. Huerta, Deep Learning for real-time gravitational wave detection and parameter estimation: Results with Advanced LIGO data, Phys. Lett. B **778**, 64 (2018).
[12] A. Menéndez-Vázquez, M. Kolstein, M. Martínez, and Ll. M. Mir, Searches for compact binary coalescence events using neural networks in the LIGO/Virgo second observation period, Phys. Rev. D **103**, 062004 (2021).
[13] E. Huerta, A. Khan, X. Huang, M. Tian, M. Levental, R. Chard, W. Wei, M. Heflin, D. S. Katz, V. Kindratenko *et al.*, Accelerated, scalable and reproducible AI-driven gravitational wave detection, Nat. Astron. **5**, 1062 (2021).
[14] M. B. Schäfer *et al.*, First machine learning gravitational-wave search mock data challenge, Phys. Rev. D **107**, 023021 (2023).
[15] R. Qiu, P. Krastev, K. Gill, and E. Berger, Deep Learning Detection and Classification of Gravitational Waves from Neutron Star-Black Hole Mergers, arXiv:2210.15888.
[16] P. Chaturvedi, A. Khan, M. Tian, E. Huerta, and H. Zheng, Inference-Optimized AI and High Performance Computing for Gravitational Wave Detection at Scale, Front. Artif. Intell. **5**, 828672 (2022).
[17] Y. Zhang, H. Xu, M. Liu, C. Liu, Y. Zhao, and J. Zhu, Deep learning model based on a bidirectional gated recurrent unit for the detection of gravitational wave signals, Phys. Rev. D **106**, 122002 (2022).
[18] M. Razzano and E. Cuoco, Image-based deep learning for classification of noise transients in gravitational wave detectors, Classical Quantum Gravity **35**, 095016 (2018).
[19] R. Biswas, L. Blackburn, J. Cao, R. Essick, K. A. Hodge, E. Katsavounidis, K. Kim, Y.-M. Kim, E.-O. Le Bigot, C.-H. Lee *et al.*, Application of machine learning algorithms to the study of noise artifacts in gravitational wave data, Phys. Rev. D **88**, 062003 (2013).
[20] M. Cavaglia, K. Staats, and T. Gill, Finding the Origin of Noise Transients in LIGO Data with Machine Learning, Commun. Comput. Phys. **25**, 963 (2019).
[21] H. Yu and R. X. Adhikari, Nonlinear Noise Cleaning in Gravitational-Wave Detectors with Convolutional Neural Networks, Front. Artif. Intell. **5**, 811563 (2022).

[22] S. Hawking, Gravitationally Collapsed Objects of Very Low Mass, Mon. Not. R. Astron. Soc. **152**, 75 (1971).
[23] B. J. Carr and S. W. Hawking, Black Holes in the Early Universe, Mon. Not. R. Astron. Soc. **168**, 399 (1974).
[24] G. Hütsi, M. Raidal, and H. Veermäe, Small-scale structure of primordial black hole dark matter and its implications for accretion, Phys. Rev. D **100**, 083016 (2019).
[25] G. Hütsi, M. Raidal, V. Vaskonen, and H. Veermäe, Two populations of LIGO-Virgo black holes, J. Cosmol. Astropart. Phys. 03 (2021) 068.
[26] G. D'Amico, P. Panci, A. Lupi, S. Bovino, and J. Silk, Massive black holes from dissipative dark matter, Mon. Not. R. Astron. Soc. **473**, 328 (2018),
[27] M. Y. Khlopov, Primordial black holes, Res. Astron. Astrophys. **10**, 495 (2010).
[28] K. Belotsky, A. Dmitriev, E. Esipova, V. Gani, A. Grobov, M. Y. Khlopov, A. Kirillov, S. Rubin, and I. Svadkovsky, Signatures of primordial black hole dark matter, Mod. Phys. Lett. A **29**, 1440005 (2014).
[29] S. Shandera, D. Jeong, and H. S. G. Gebhardt, Gravitational Waves From Binary Mergers of Subsolar Mass Dark Black Holes, Phys. Rev. Lett. **120**, 241102 (2018).
[30] C. Kouvaris and P. Tinyakov, Constraining asymmetric dark matter through observations of compact stars, Phys. Rev. D **83**, 083512 (2011),
[31] D. J. Kaup, Klein-Gordon Geon, Phys. Rev. **172**, 1331 (1968).
[32] H.-K. Guo, K. Sinha, and C. Sun, Probing boson stars with extreme mass ratio inspirals, J. Cosmol. Astropart. Phys. 09 (2019) 032.
[33] M. Colpi, S. L. Shapiro, and I. Wasserman, Boson Stars: Gravitational Equilibria of Self-Interacting Scalar Fields, Phys. Rev. Lett. **57**, 2485 (1986).
[34] R. Abbott *et al.* (LIGO Scientific Collaboration and Virgo Collaboration), Search for Subsolar-Mass Binaries in the First Half of Advanced LIGO's and Advanced Virgo's Third Observing Run, Phys. Rev. Lett. **129**, 061104 (2022).
[35] A. H. Nitz and Y.-F. Wang, Broad search for gravitational waves from subsolar-mass binaries through LIGO and Virgo's third observing run, Phys. Rev. D **106**, 023024 (2022).
[36] B. Abbott *et al.* (LIGO Scientific Collaboration, KAGRA Collaboration and Virgo Collaboration), Search for subsolar-mass black hole binaries in the second part of Advanced LIGO's and Advanced Virgo's third observing run, arXiv:2212.01477.
[37] A. H. Nitz and Y.-F. Wang, Search for Gravitational Waves from the Coalescence of Subsolar Mass and Eccentric Compact Binaries, Astrophys. J. **915**, 54 (2021).
[38] A. H. Nitz and Y.-F. Wang, Search for Gravitational Waves from High-Mass-Ratio Compact-Binary Mergers of Stellar Mass and Subsolar Mass Black Holes, Phys. Rev. Lett. **126**, 021103 (2021).
[39] K. S. Phukon, G. Baltus, S. Caudill, S. Clesse, A. Depasse, H. Fong, S. J. Kapadia, R. Magee, and A. J. Tanasijczuk, The hunt for sub-solar primordial black holes in low mass ratio binaries is open, arXiv:2105.11449.
[40] R. Abbott *et al.* (LIGO Scientific Collaboration and Virgo Collaboration), Search for Subsolar Mass Ultracompact Binaries in Advanced LIGO's Second Observing Run, Phys. Rev. Lett. **123**, 161102 (2019).
[41] D. Davis *et al.* (LIGO Scientific Collaboration), LIGO detector characterization in the second and third observing runs, Classical Quantum Gravity **38**, 135014 (2021).
[42] F. Acernese *et al.* (Virgo Collaboration), Virgo Detector Characterization and Data Quality during the O3 run, arXiv:2205.01555.
[43] S. A. Usman, A. H. Nitz, I. W. Harry, C. M. Biwer, D. A. Brown, M. Cabero, C. D. Capano, T. D. Canton, T. Dent, S. Fairhurst *et al.*, The PyCBC search for gravitational waves from compact binary coalescence, Classical Quantum Gravity **33**, 215004 (2016).
[44] A. H. Nitz, T. Dent, T. Dal Canton, S. Fairhurst, and D. A. Brown, Detecting Binary Compact-Object Mergers with Gravitational Waves: Understanding and Improving the Sensitivity of the PyCBC Search, Astrophys. J. **849**, 118 (2017).
[45] A. Nitz, I. Harry, D. Brown, C. M. Biwer, J. Willis, T. Dal Canton, C. Capano, L. Pekowsky, T. Dent, A. R. Williamson *et al.*, gwastro/pycbc: PyCBC release v1.16.11 (Zenodo, 2020), 10.5281/zenodo.4134752.
[46] S. Husa, S. Khan, M. Hannam, M. Pürrer, F. Ohme, X. J. Forteza, and A. Bohé, Frequency-domain gravitational waves from nonprecessing black-hole binaries. I. New numerical waveforms and anatomy of the signal, Phys. Rev. D **93**, 044006 (2016).
[47] S. Khan, S. Husa, M. Hannam, F. Ohme, M. Pürrer, X. J. Forteza, and A. Bohé, Frequency-domain gravitational waves from nonprecessing black-hole binaries. II. A phenomenological model for the advanced detector era, Phys. Rev. D **93**, 044007 (2016).
[48] B. P. Abbott *et al.* (LIGO Scientific Collaboration and Virgo Collaboration), A guide to LIGO–Virgo detector noise and extraction of transient gravitational-wave signals, Classical Quantum Gravity **37**, 055002 (2020).
[49] J. C. Brown, Calculation of a constant Q spectral transform, J. Acoust. Soc. Am. **89**, 425 (1991).
[50] J. C. Brown and M. S. Puckette, An efficient algorithm for the calculation of a constant Q transform, J. Acoust. Soc. Am. **92**, 2698 (1992).
[51] C. Schörkhuber and A. Klapuri, Constant-q transform toolbox for music processing, in *7th Sound and Music Computing Conference, Barcelona, Spain* (SMC, 2010), pp. 3–64.
[52] S. Ioffe and C. Szegedy, Batch Normalization: Accelerating Deep Network Training by Reducing Internal Covariate Shift, arXiv:1502.03167v3.
[53] K. He, X. Zhang, S. Ren, and J. Sun, Deep residual learning for image recognition, in *Proceedings of the IEEE Conference on Computer Vision and Pattern Recognition* (IEEE, 2016), pp. 770–778.
[54] K. He, X. Zhang, S. Ren, and J. Sun, Identity Mappings in Deep Residual Networks, arXiv:1603.05027.
[55] D. P. Kingma and J. L. Ba, Adam: A Method for Stochastic Optimization, arXiv:1412.6980.
[56] S. Ruder, An overview of gradient descent optimization algorithms, arXiv:1609.04747.
[57] I. Goodfellow, Y. Bengio, and A. Courville, *Deep Learning* (MIT Press, Cambridge, MA, 2016), https://www.deeplearningbook.org/.
[58] M. Abadi, P. Barham, J. Chen, Z. Chen, A. Davis, J. Dean, M. Devin, S. Ghemawat, G. Irving, M. Isard *et al.*,

TensorFlow: A system for LargeScale machine learning. In 12th USENIX symposium on operating systems design and implementation (OSDI 16), in *12th USENIX Symposium on Operating Systems Design and Implementation (OSDI 16)* (USENIX, 2016), pp. 265–283.

[59] R. Abbott *et al.* (LIGO Scientific Collaboration and Virgo Collaboration), Search for gravitational waves from galactic and extra-galactic binary neutron stars, Phys. Rev. D **72**, 082001 (2005).

[60] T. B. Littenberg, J. B. Kanner, N. J. Cornish, and M. Millhouse, Enabling high confidence detections of gravitational-wave bursts, Phys. Rev. D **94**, 044050 (2016).

[61] Y. S. C. Lee, M. Millhouse, and A. Melatos, Enhancing the gravitational-wave burst detection confidence in expanded detector networks with the BayesWave pipeline, Phys. Rev. D **103**, 062002 (2021).

[62] V. Tiwari, Estimation of the sensitive volume for gravitational-wave source populations using weighted Monte Carlo integration, Classical Quantum Gravity **35**, 145009 (2018).

[63] A. H. Nitz and Y. F. Wang, Search for Gravitational Waves from the Coalescence of Subsolar-Mass Binaries in the First Half of Advanced LIGO and Virgo's Third Observing Run, Phys. Rev. Lett. **127**, 151101 (2021).